Effect of respiratory motion on internal radiation dosimetry

Tianwu Xie
Division of Nuclear Medicine and Molecular Imaging, Geneva University Hospital, Geneva 4 CH-1211, Switzerland

Habib Zaidi[a)]
Division of Nuclear Medicine and Molecular Imaging, Geneva University Hospital, Geneva 4 CH-1211, Switzerland; Geneva Neuroscience Center, Geneva University, Geneva CH-1205, Switzerland; and Department of Nuclear Medicine and Molecular Imaging, University of Groningen, University Medical Center Groningen, Groningen 9700 RB, The Netherlands

(Received 2 June 2014; revised 27 September 2014; accepted for publication 29 September 2014; published 23 October 2014)

Purpose: Estimation of the radiation dose to internal organs is essential for the assessment of radiation risks and benefits to patients undergoing diagnostic and therapeutic nuclear medicine procedures including PET. Respiratory motion induces notable internal organ displacement, which influences the absorbed dose for external exposure to radiation. However, to their knowledge, the effect of respiratory motion on internal radiation dosimetry has never been reported before.
Methods: Thirteen computational models representing the adult male at different respiratory phases corresponding to the normal respiratory cycle were generated from the 4D dynamic XCAT phantom. Monte Carlo calculations were performed using the MCNP transport code to estimate the specific absorbed fractions (SAFs) of monoenergetic photons/electrons, the *S*-values of common positron-emitting radionuclides (C-11, N-13, O-15, F-18, Cu-64, Ga-68, Rb-82, Y-86, and I-124), and the absorbed dose of ^{18}F-fluorodeoxyglucose (^{18}F-FDG) in 28 target regions for both the static (average of dynamic frames) and dynamic phantoms.
Results: The self-absorbed dose for most organs/tissues is only slightly influenced by respiratory motion. However, for the lung, the self-absorbed SAF is about 11.5% higher at the peak exhale phase than the peak inhale phase for photon energies above 50 keV. The cross-absorbed dose is obviously affected by respiratory motion for many combinations of source-target pairs. The cross-absorbed *S*-values for the heart contents irradiating the lung are about 7.5% higher in the peak exhale phase than the peak inhale phase for different positron-emitting radionuclides. For ^{18}F-FDG, organ absorbed doses are less influenced by respiratory motion.
Conclusions: Respiration-induced volume variations of the lungs and the repositioning of internal organs affect the self-absorbed dose of the lungs and cross-absorbed dose between organs in internal radiation dosimetry. The dynamic anatomical model provides more accurate internal radiation dosimetry estimates for the lungs and abdominal organs based on realistic modeling of respiratory motion. This work also contributes to a better understanding of model-induced uncertainties in internal radiation dosimetry. © *2014 American Association of Physicists in Medicine.* [http://dx.doi.org/10.1118/1.4898118]

Key words: radiation dosimetry, PET, Monte Carlo, respiratory motion, simulation

1. INTRODUCTION

A number of computational models have been developed to mimic the physical characteristics and interior and exterior anatomical features of human body. These models were extensively used in internal and external radiation dosimetry calculations for radiation protection and therapeutic nuclear medicine procedures as well as multimodality imaging physics research.[1] According to the geometric features used to define the anatomical structures of the human body, computational phantoms can be divided into three types: stylized models which employ simple equation-based mathematical functions, voxel-based models which use matrices obtained from segmented cryosection or medical (CT or MR) images, and hybrid equationvoxel-based models which combine the two aforementioned modeling approaches. Monte Carlo-based dose calculation involves the use of a computational model as input to a dedicated Monte Carlo package (e.g., MCNP, EGS, GEANT4, etc.) that simulates particle transport in biological tissues. This approach is considered to be one of the most accurate methods for absorbed dose estimation.[2,3] The reliability of the Monte Carlo method is strongly dependent on the adopted computational model which reflects the physical characteristics (elemental composition, mass density, etc.) and anatomical features (shape, density, volume, and position of organs and tissues) of the human body.

In most radiation dosimetry studies, dose calculations are based on static computational phantoms, where the physical characteristics and anatomical features of organs and tissues of the model are defined and remain constant. However, under

realistic conditions, respiratory motion leads to notable temporal and spatial anatomic changes of internal organs located in the thorax and upper abdomen, which might impact the absorbed dose distribution. Respiration-induced dosimetry errors have been reported to critically influence the radiation dose estimation in external exposure to radiation.[4,5] However, the effect of respiratory motion on internal radiation dosimetry has not yet been investigated.

As one of the most radiosensitive and important dose-limiting organs, the lung is assigned a tissue weighting factor of 0.12 for calculation of effective dose in the 2007 recommendations of the ICRP.[6] The exposure of the lungs to ionizing radiation may cause immediate or latent pulmonary injury and raises the risk of lung cancer.[7,8] Under rest conditions, the change of lung volume during respiration is about 10% from the start to the end of inhalation.[9] As such, an investigation of the variability in internal dose calculations across the human respiratory cycle is recommended given its relevance for providing accurate assessment of lung dose and understanding the uncertainty in the reported dosimetric estimates.

In the Medical Internal Radionuclide Dose Committee (MIRD) formalism, the radiation absorbed dose $D(r_T,T_D)$ delivered to any target tissue r_T from source organ r_S, over a considered dose-integration period T_D, is given by[10]

$$D(r_T,T_D)=\sum_{r_S}\int_0^{T_D}A(r_S,t)S(r_T\leftarrow r_S,t)dt, \quad (1)$$

where $A(r_S,t)$ is the time-dependent activity of the radiotracer in the source region and $S(r_T\leftarrow r_S,t)$ is the time-dependent S-value describing the dose rate in the target organ per unit activity in the source organ. In most reported dosimetry studies, the S-value is obtained from static computational models and is assumed to be constant during the period of interest. In the static conditions, Eq. (1) can be rewritten as

$$D(r_T,T_D)=\sum_{r_S}\tilde{A}(r_S,T_D)S(r_T\leftarrow r_S), \quad (2)$$

where $\tilde{A}(r_S,T_D)$ is the cumulated (time-integrated) activity of the radiotracer in the source region and $S(r_T\leftarrow r_S)$ is the time-independent S-value of the static model.

In this work, we investigated the effect of respiratory motion on internal radiation dosimetry in the adult man for monoenergetic photons and electrons and common positron-emitting radionuclides. The XCAT nonuniform rational b-spline (NURBS)-based 4D model was used to produce a series of computational models representing the human body at 13 different respiratory frames of the normal respiration cycle. Monte Carlo-based particle transport simulations of monoenergetic photons/electrons and spectra corresponding to decay schemes of common positron-emitting radionuclides (C-11, N-13, O-15, F-18, Cu-64, Ga-68, Rb-82, Y-86, and I-124) were performed using MCNPX to calculate the absorbed fractions (AFs), specific absorbed fractions (SAFs), and S-values for the considered series of models. The absorbed organ doses of ^{18}F-fluorodeoxyglucose (^{18}F-FDG) were also calculated according to the MIRD schema and published biodistribution data. The discrepancy of dosimetric results between static and dynamic models was then evaluated to characterize the uncertainties involved in internal radiation dosimetry calculations.

2. MATERIALS AND METHODS

2.A. Computational phantoms

The XCAT NURBS-based 4D phantom was used in this work to generate 13 computational voxel-based models representing the adult human body at different respiratory phases of the normal respiration cycle. The time-dependent movements of the diaphragm and ribcage during respiratory motion were extracted by analyzing several sets of 4D respiratory-gated CT image data of patients and were integrated in the 4D-XCAT phantom to define the expansion of the chest and motion of the diaphragm at a given time point of the respiratory cycle.[2,11] The heart, liver, stomach, spleen, and kidneys moved with scaled down motions from that of the diaphragm and were used to setup a motion vector field for the modification of the other structures.[2,11] The length of the considered respiratory cycle was 5.2 s under normal breathing conditions. The extent of diaphragmatic motion and the anteroposterior expansion of the chest were 2 and 0.5 cm, respectively. Twenty-eight identified target regions were considered in the calculations. The 13 generated voxel-based phantoms were numbered as respiratory frame I–XIII. A static phantom representing the average model over one respiratory cycle was also produced by averaging the 13 models generated at different respiratory phases using a c++ code developed in-house. The organ masses and body weights of the static phantom and the phantoms corresponding to respiratory frames I (start of inhalation) and VI (end of inhalation) are summarized in Table I. The same organs/tissues in the static and dynamic phantoms have comparable masses while the volume of the lung in the dynamic phantom varies across the different respiratory phases. The minor discrepancy between masses of same organs within the different phantoms can be attributed to respiratory-induced repositioning and deformation of internal organs. The relative standard deviation of organ masses among the different phantoms is less than 0.1% for most organs. Figure 1 shows 3D images of the whole body and thoracic/abdominal organs of the static and dynamic phantoms at respiratory phases I and VI. A c++ code developed in-house was used to calculate the average distances between organs in the voxel-based phantoms. Table II lists the average distances between selected organs of the static phantom. The mean distance was calculated by averaging the Euclidean distance of corresponding voxel pairs of the selected organs. The changes of selected source-target organ distances of the dynamic phantoms from peak exhale phase to peak inhale phase are listed in Table III.

2.B. Monte Carlo simulations and dosimetry calculations

The generated computational models were used as input to the MCNPX Monte Carlo code[12] to simulate the transport

TABLE I. Organ masses and total body weights of the static phantoms and selected respiratory frames of the dynamic phantoms.

	Mass (g)			Volume (cm^3)		
		Dynamic phantoms			Dynamic phantoms	
Identified organs	Static phantoms	Respiratory phase I (Start of inhalation)	Respiratory phase VI (End of inhalation)	Static phantoms	Respiratory phase I (Start of inhalation)	Respiratory phase VI (End of inhalation)
Remainder	51 290	51 248	51 365	57 372	56 942	57 073
Adrenal	21	21	21	21	21	21
Brain	1574	1574	1574	1513	1513	1513
Colon	1087	1088	1089	1025	1056	990
Gall bladder	71	72	71	71	70	72
Heart wall	188	188	188	177	177	177
Heart contents	389	389	389	367	367	367
Kidney	365	365	366	332	351	324
Liver	1813	1810	1812	1777	1774	1776
Lungs	1198	1201	1200	3257	2974	3561
Pancreas	144	144	145	141	140	144
Small intestine	1450	1451	1451	1368	1409	1319
Spinal cord	42	42	42	41	41	41
Spleen	179	179	178	169	169	168
Stomach	417	417	418	405	405	406
Salivary glands	113	113	113	110	110	110
Thymus	33	33	33	37	32	42
Thyroid	28	28	28	27	27	28
Urinary bladder	55	55	55	51	53	49
Cortical bone	5455	5446	5488	4102	4064	4095
Bone marrow	3632	3640	3640	3493	3500	3500
Testes	41	41	41	39	39	39
Prostate	19	19	19	18	18	18
Cartilage	342	342	341	278	285	282
Esophagus	48	48	48	48	46	52
Larynx and pharynx	41	41	41	39	39	39
Skin	3313	3303	3313	3898	3886	3897
Eye balls	19	19	19	19	19	19
Total body	73 (kg)	73 (kg)	73 (kg)	80 ($10^3 \times cm^3$)	80 ($10^3 \times cm^3$)	80 ($10^3 \times cm^3$)

and interaction of emitted radiation. The number of voxels of each identified region was calculated and multiplied by the voxel volume ($0.2 \times 0.2 \times 0.6$ cm^3) and corresponding tissue density to yield the region mass. The chemical composition of each organ was obtained from ICRP publications.[9] The simulations included two independent parts: (1) simulation of monoenergetic photons and electrons and (2) simulation for positron-emitting radionuclides. In the first part, monoenergetic photons and electrons were generated from 14 identified organs [including the remainder, colon, heart wall, heart contents, kidney, liver, lung, pancreas, small intestine (SI), spleen, stomach, thymus, thyroid, and urinary bladder (UB)] with 20 discrete photon energies ranging from 0.01 to 3.0 MeV and 13 selected electron energies ranging from 0.1 to 3.0 MeV. The SAFs, reflecting the mass averaged proportion of energy released in source organs and deposited in the target organ, were calculated for all organs of the 14 computational models (including the static model and 13 models corresponding to different respiratory phases). Thereafter, these estimates were compared to similar quantities calculated for the computational models at respiratory phases I and VI as well as models developed by Stabin and Siegel[13] and Chao.[14] Photon and electron SAFs for selected organs/tissues in the static and dynamic phantoms were then analyzed. In the second part, we simulated uniformly distributed positron-emitting radionuclides (C-11, N-13, O-15, F-18, Cu-64, Ga-68, Rb-82, Y-86, and I-124) in 28 identified organs (Table I) of the 14 generated computational models. Their decay schemes were obtained from the Health Physics Society electronic resource.[15] *S*-values of the considered radionuclides were calculated for all source-target pairs of 14 models. In all simulations, a total of 1.0×10^7 primary particle histories were generated such that the statistical uncertainty in terms of coefficient of variation (COV) was less than 2% in most cases.

In this work, the *S*-values of F-18 of the 4D phantom datasets and the static phantom were employed for absorbed dose calculations of ^{18}F-FDG in an adult male according to Eqs. (1) and (2), respectively. The time-dependent distribution kinetics of ^{18}F-FDG in the human body were obtained from the MIRD pamphlet 19.[16] The effective doses of ^{18}F-FDG can be calculated by the sum of the product of tissue weighting factors and equivalent doses obtained by multiplying the absorbed dose and radiation weighting factors.[10]

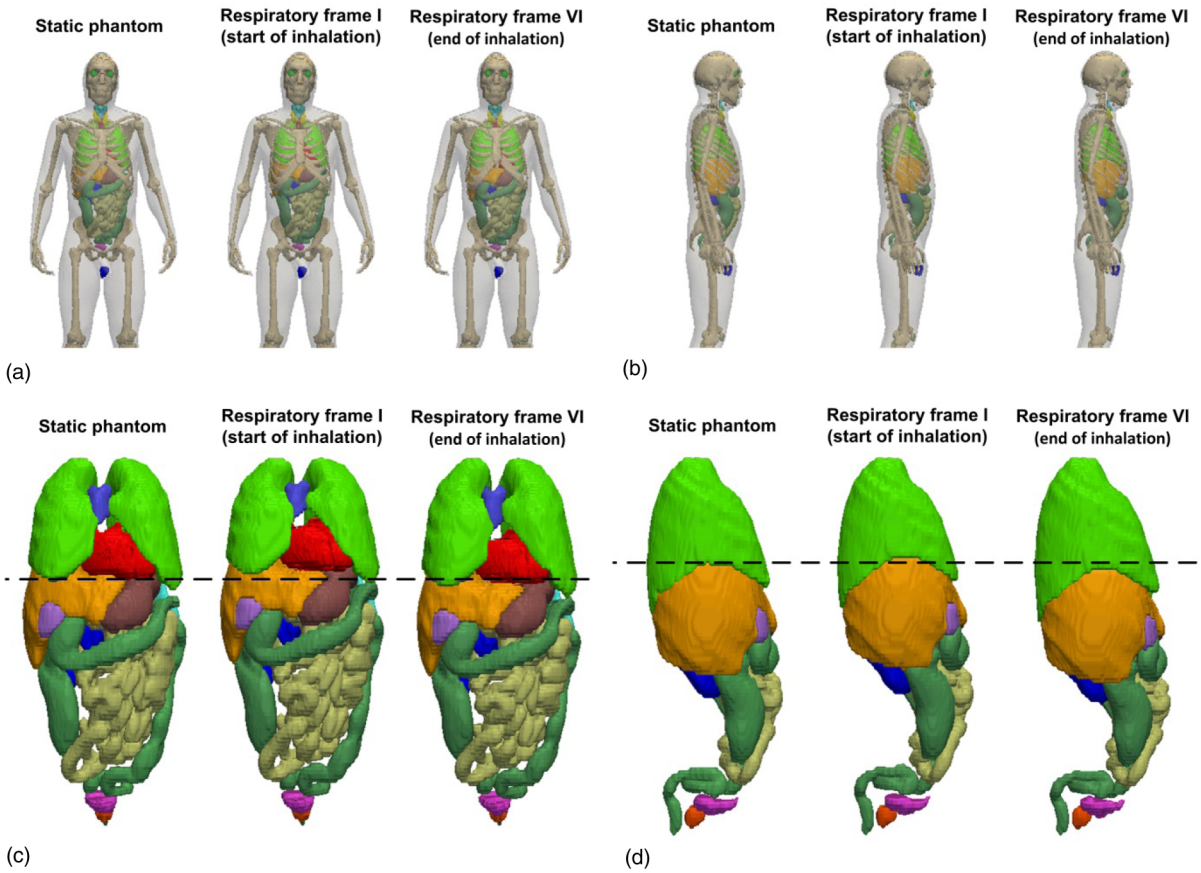

FIG. 1. 3D visualization of static and dynamic phantoms showing (a) front views and (b) side views of the static phantom and the phantoms corresponding to respiratory frames I and VI. (c) The front views and (d) the side views of thoracic and abdominal organs of the static phantom and the phantoms corresponding to respiratory frames I and VI.

3. RESULTS AND DISCUSSION

3.A. Modeling of respiratory motion in the dynamic phantoms

To calculate the radiation dose distributions in the human body corresponding to the different respiratory phases, the dynamic 4D-XCAT phantom was treated as a combination of a series of 3D models representing the anatomy at each phase of the respiratory cycle. By converting the NURBS surfaces to voxels for each respiratory phase, a series of voxel-based 3D phantoms were generated from the 4D-XCAT phantom for Monte Carlo-based particle transport simulations. The uniform time interval between each frame was 0.4 s. A total of 13 voxel-based computational models with matrix size of $326 \times 132 \times 300$ were sampled and generated to represent a normal respiratory cycle at rest. The models of respiratory phases I and VI represent the peak exhale phase (start of inhalation) and peak inhale phase (end of inhalation), respectively. The voxel resolution of each computational phantom was $2 \times 2 \times 6$ mm for the x, y, and z axes, respectively. The masses of the same organs between each adopted voxel-based model, including the static phantom, were constant (Table I). The density of the lung in each computational model was obtained by dividing organ mass by the corresponding lung volume, which changes during the respiratory cycle. The averaged voxel distances between major visceral organs were calculated for the frames I and VI, and the percentage changes of organ distances from the peak exhale phase to the peak inhale phase were calculated and analyzed. As can be seen in Table III, in normal respiratory cycle of the dynamic phantom, the average voxel distances from lung to gall bladder (GB), heart, adrenal, kidney, spleen, stomach, and pancreas increased by 2.3%–5.2% from the peak exhale phase to the peak inhale phase because of the anteroposterior expansion of the chest. The average voxel distances from the lung to thymus and thyroid increased by 2.7%–4.6%, and the distance from the lung to colon, liver, SI, UB, testes, and prostate decreased by 1.6%–11.2% because of the lung expansion along the direction of diaphragmatic motion. For organs in the abdominal cavity, the cross distances in 82% of the considered source-target organ pairs were reduced during the inhalation. For the UB, one of the major source organs for many radiopharmaceuticals, the cross-organ distance to superior abdominal organs (such as the colon, SI, stomach, and spleen) was reduced by 4.4%–5.7%, which may increase the UB-induced cross-absorbed radiation dose in these target organs.

TABLE II. Average distances between selected organs in the static phantom.

Distances (cm)	Adrenal	Colon	Gall bladder	Heart wall	Heart contents	Kidney	Liver	Lung	Pancreas	Small intestine	Spleen	Stomach	Thymus	Thyroid	Urinary bladder	Testes
Colon	16.7	—	—	—	—	—	—	—	—	—	—	—	—	—	—	—
Gall bladder	11.9	17.7	—	—	—	—	—	—	—	—	—	—	—	—	—	—
Heart wall	14.2	22.8	14.8	—	—	—	—	—	—	—	—	—	—	—	—	—
Heart contents	14.4	23.2	14.5	6.3	—	—	—	—	—	—	—	—	—	—	—	—
Kidney	8.8	16.0	14.6	18.5	18.9	—	—	—	—	—	—	—	—	—	—	—
Liver	11.4	20.0	9.5	15.3	14.9	14.5	—	—	—	—	—	—	—	—	—	—
Lung	18.0	17.8	19.5	11.3	12.4	23.5	11.5	—	—	—	—	—	—	—	—	—
Pancreas	6.7	15.6	10.3	12.4	12.9	10.1	11.9	18.1	—	—	—	—	—	—	—	—
Small intestine	14.5	11.1	16.2	21.1	21.1	14.4	15.4	13.2	12.7	—	—	—	—	—	—	—
Spleen	11.0	20.2	20.2	14.8	15.7	12.7	19.0	18.6	11.3	17.8	—	—	—	—	—	—
Stomach	10.9	19.8	14.3	9.6	10.4	14.3	15.2	16.0	9.0	17.2	10.6	—	—	—	—	—
Thymus	20.3	30.6	18.8	9.7	8.5	24.9	18.7	11.7	19.1	28.6	21.6	16.2	—	—	—	—
Thyroid	29.8	40.6	28.8	18.9	17.8	34.4	28.0	17.2	29.1	38.8	29.7	25.4	10.8	—	—	—
Urinary bladder	28.3	19.7	30.6	39.3	40.0	25.1	32.1	43.9	28.4	20.4	32.2	33.7	46.6	56.8	—	—
Testes	39.5	29.2	40.7	49.6	50.4	36.0	42.8	54.6	39.1	29.8	42.8	43.9	57.1	67.4	12.2	—
Prostate	30.0	21.6	33.1	41.5	42.2	26.6	34.1	45.6	30.5	23.0	33.5	35.8	48.9	58.9	4.5	12.1

TABLE III. Relative changes of selected organ distances from respiratory phases I to VI.

	Percentage differences (%) of organ distances from respiratory frames I to VI														
Organs	Adrenal	Colon	Gall bladder	Heart	Kidney	Liver	Lung	Pancreas	Small intestine	Spleen	Stomach	Thymus	Thyroid	Urinary bladder	Testes
Colon	−2.9	—	—	—	—	—	—	—	—	—	—	—	—	—	—
Gall bladder	0.0	−2.7	—	—	—	—	—	—	—	—	—	—	—	—	—
Heart	0.2	−3.1	−0.1	—	—	—	—	—	—	—	—	—	—	—	—
Kidney	−2.7	−2.5	−1.2	−1.4	—	—	—	—	—	—	—	—	—	—	—
Liver	0.6	1.0	0.3	0.3	−1.4	—	—	—	—	—	—	—	—	—	—
Lung	5.2	−5.6	3.7	2.3	4.5	−11.2	—	—	—	—	—	—	—	—	—
Pancreas	−0.1	−2.7	0.6	−0.6	−1.4	0.7	4.0	—	—	—	—	—	—	—	—
Small intestine	−2.7	5.3	−2.2	4.2	−2.7	8.6	−5.0	−2.7	—	—	—	—	—	—	—
Spleen	−0.1	−2.3	0.0	0.4	−1.6	0.4	4.3	−1.0	−3.6	—	—	—	—	—	—
Stomach	−0.4	−2.3	−0.1	−0.3	−1.5	0.3	3.4	−1.0	−1.9	0.0	—	—	—	—	—
Thymus	3.3	0.2	2.8	5.5	1.2	3.3	2.7	2.6	0.7	2.7	2.8	—	—	—	—
Thyroid	6.3	3.5	6.9	10.8	4.3	6.7	4.6	6.2	4.3	5.8	7.2	13.7	—	—	—
Urinary bladder	−5.7	−5.2	−4.9	−3.9	−5.0	−4.8	−1.6	−5.1	−5.3	−4.9	−4.4	−2.2	−0.5	—	—
Testes	−5.1	−5.1	−4.7	−3.9	−4.6	−4.5	−1.9	−4.8	−5.2	−4.7	−4.4	−2.5	−0.1	−3.2	—
Prostate	−5.8	−5.0	−4.6	−3.9	−5.2	−4.8	−1.8	−5.1	−4.9	−5.1	−4.5	−2.3	0.2	−1.4	−1.6

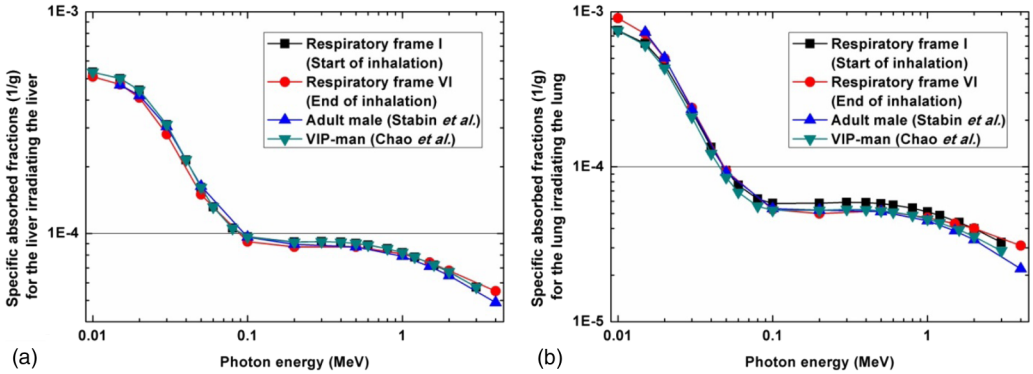

FIG. 2. Comparison of photon self-SAFs for (a) the liver and (b) the lung between the phantoms corresponding to respiratory frames I and VI in this work and Chao (Ref. 14) and Stabin and Siegel (Ref. 13).

3.B. Specific absorbed fractions for photons and electrons

The SAFs for monoenergetic photons and electrons for 392 selected source-target organ pairs were calculated. Figure 2 shows the self-SAFs for photon sources in the liver and lung at respiratory frames I and VI. Comparisons with the results of Chao[14] and Stabin and Siegel[13] are also given. The self-SAFs estimated among the different computational models are in close agreement.

The changes in the SAFs over the normal respiratory cycle were estimated and analyzed for the static computational phantom and at each respiratory phase of the dynamic phantom. Figure 3 shows ratios of photon and electron SAFs of computational models in various respiratory phases (from respiratory frames I to VI) to the static model for the self-irradiation of lung and stomach. Except for the lungs, the self-SAFs of most organs in the models corresponding to different respiratory phases are identical to those of the static model [Figs. 3(c) and 3(d)]. For the lung, the self-SAF at each source energy decreases from the peak exhale phase (respiratory frame I) to the peak inhale phase (respiratory phase VI) and presents significant respiration-induced variations during inhalation, because the inspired air reduces the average density of the whole lung, thus facilitating the escape of recoil electrons and scattered photons from the lung tissue and reducing the amount of energy deposition of secondary particles in the lung. For photon energies lower than 30 keV and electron energies lower than 1.2 MeV, the self-SAFs for the lung are less influenced by respiratory motion. As can be seen in Fig. 3(a), when the photon energy is above 50 keV, the self-SAF of the lung is about 11.5%

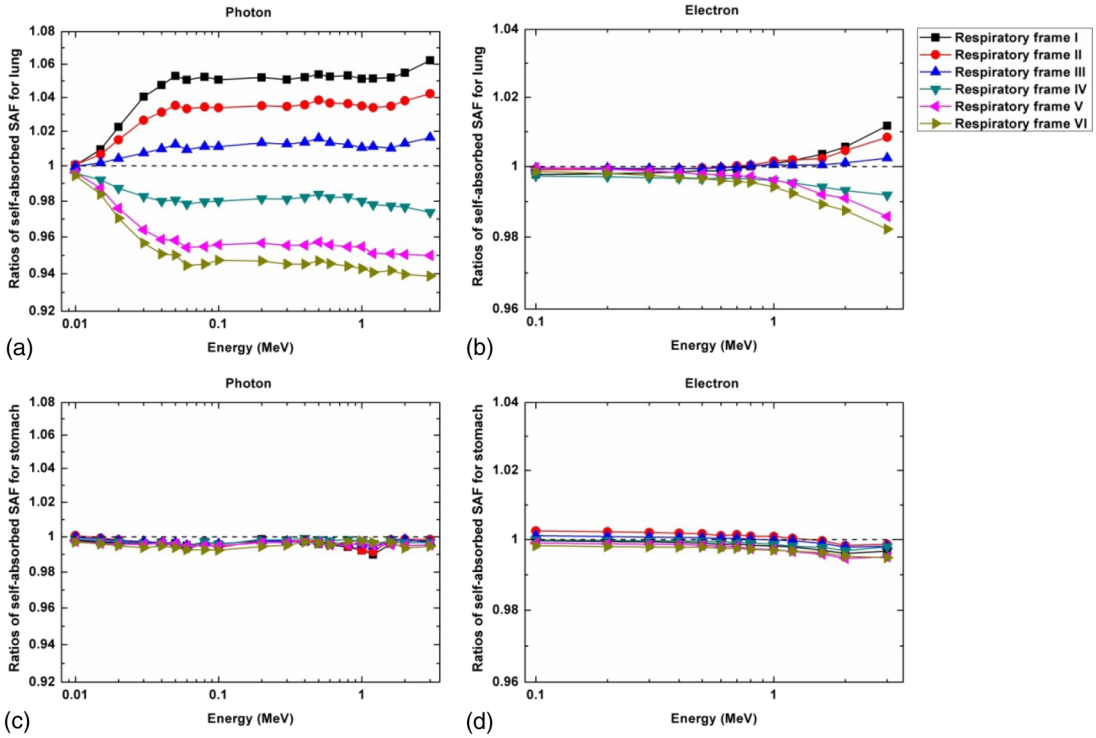

FIG. 3. Ratios of (a) photon and (b) electron self-SAFs of the lung and (c) photon and (d) electron self-SAFs of the stomach from dynamic phantoms at respiratory frames I, II, III, IV, V, and VI to the static phantom.

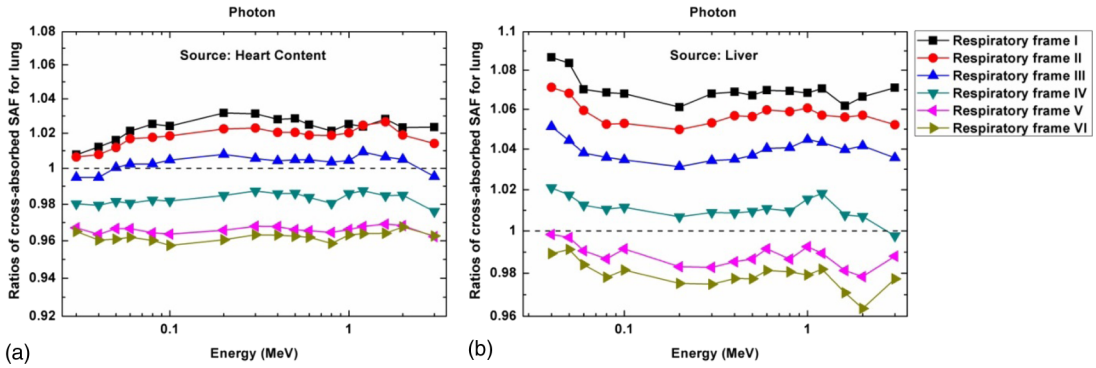

FIG. 4. Ratios of cross-SAFs of photons for (a) the heart contents irradiating the lung and (b) the liver irradiating the lung from computational phantoms at respiratory frames I, II, III, IV, V, and VI to the static phantom.

higher in the peak exhale phase (respiratory frame I) and 5.9% higher in the static model compared to the peak inhale phase (respiratory frame VI), since higher energy particles are more sensitive to respiration-induced changes of the lung density than lower energy particles.

Figure 4 shows the ratios of cross-SAFs for the heart and liver irradiating the lung among computational models at various respiratory phases (from respiratory frames I to VI) and the static model. The average relative differences of photon cross-SAFs for the heart or liver irradiating the lung among the models at peak exhale phase (respiratory frame I) and peak inhale phase (respiratory frame VI) are 6.4% and 9.6%, respectively. Similar to the self-SAFs, it was observed that the cross-SAFs for the lung also decreased during inhalation.

For other organs, there is no obvious effect of respiratory motion on the self-SAF. The influence of respiratory motion on the dose to the lung is larger for cross-irradiation than for self-irradiation.

3.C. *S*-values for positron-emitting radionuclides

The *S*-values of nine common positron-emitting radionuclides for 30 source organs irradiating 30 target organs. Figure 5 shows the self *S*-values of the liver and spleen for the static phantom and dynamic computational models at respiratory frames I and VI. Comparisons with the results obtained by Stabin and Siegel[13] are also given. As can be seen in Fig. 5, the self *S*-values of the different computational models are very similar.

Figure 6 shows the ratios of self *S*-values in the lung and liver of the dynamic phantom to the static phantom for the considered radionuclides. For the lung in normal respiratory cycle, the self *S*-values decrease during inhalation and increase during exhalation. The maxima and minima of the *S*-value curves correspond to the peak exhale phase and peak inhale phase, respectively. The self *S*-values of F-18 and Y-86 in the lung are 2.3% and 5.7% higher at the peak exhale phase than the peak inhale phase, respectively. During the respiratory cycle, the effect of respiratory motion on the self *S*-values of the lung is dependent on the decay scheme of the radionuclide, where the variation of the *S*-values curve is positively correlated with the yield of high-energy emitted photons. The effect of respiratory motion on the self *S*-values for radionuclides in other organs, such as the liver [Fig. 6(b)] is minor and barely perceptible. The self *S*-values for most organs are constant during respiration except for the lung.

Figure 7 shows the ratios of cross *S*-values of the dynamic phantom to the static phantom for the heart contents and stomach irradiating the lung, UB irradiating SI and kidney irradiating stomach. For the different positron-emitting radionuclides, the tendency of the curves of cross *S*-values for the same source-target pairs is consistent. The shape of the curve of cross *S*-values depends on the relative motion between source-target pairs during respiration. For the heart

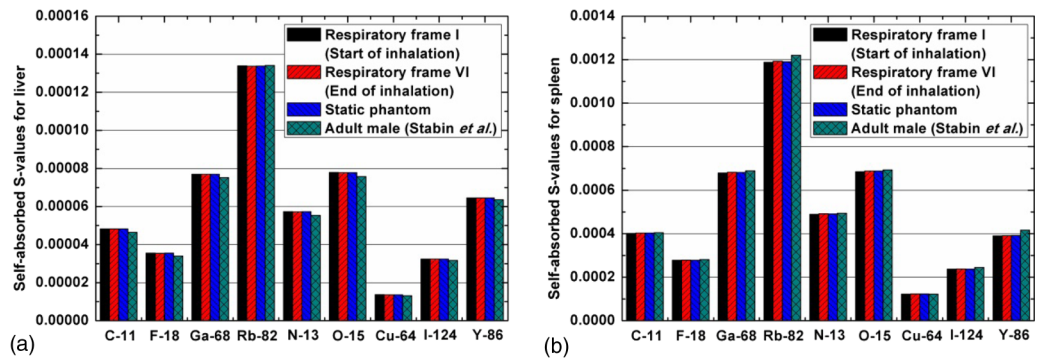

FIG. 5. Comparison of the self *S*-values of the investigated positron-emitting radionuclides for (a) the liver and (b) the spleen between this work and Stabin and Siegel (Ref. 13).

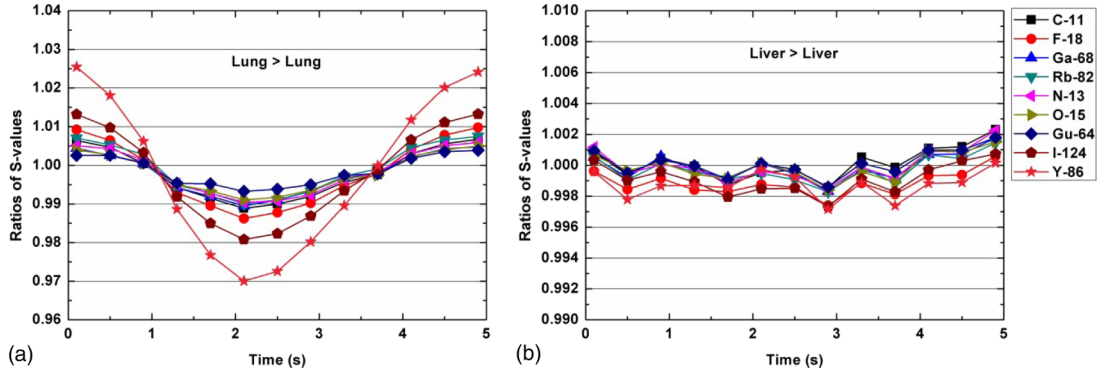

FIG. 6. Ratios of self S-values of the investigated radionuclides for (a) the lung and (b) the liver between the dynamic phantoms and the static phantoms during an average respiratory cycle of 5.2 s, starting from the beginning of inhalation to the end of exhalation.

contents and stomach irradiating the lung, the average difference between S-values in the peak exhale phase and peak inhale phase is 7.5%, whereas it is −8.7% for the UB irradiating the SI and −1.4% for the kidney irradiating the stomach. The convex S-value curves of the heart contents and stomach irradiating the lung and the concave S-value curves of the UB irradiating the SI are caused by the increased and reduced source-target distances, respectively, in the inhalation phase. For source-target pairs presenting with small changes of the distances between them during respiration, the effect of respiratory motion on the cross S-values is minor. Figure 8 shows the ratios of S-values of F-18 and C-11 of the dynamic phantom to the static phantom for representative source organs irradiating the lung. The change of cross S-values for the lung during the respiratory cycle is about 2.4–4.2 times higher than that of self S-values. For most source-target organ pairs, the ratios of S-values of the different frames corresponding to different respiratory phases of the dynamic phantom to the static phantom vary between 0.9 and 1.1.

The contribution of various types of radiation to the total S-values of different source-target organ pairs in the dynamic phantom was also calculated and analyzed. As can be seen in Fig. 9, for the S-value of the total body irradiating the lung, from the peak exhale phase to the peak inhale phase, the contribution of annihilation photons decreases with an overall average difference of −10.3%, whereas the contribution of positrons increases with an average difference of 4.1%. This

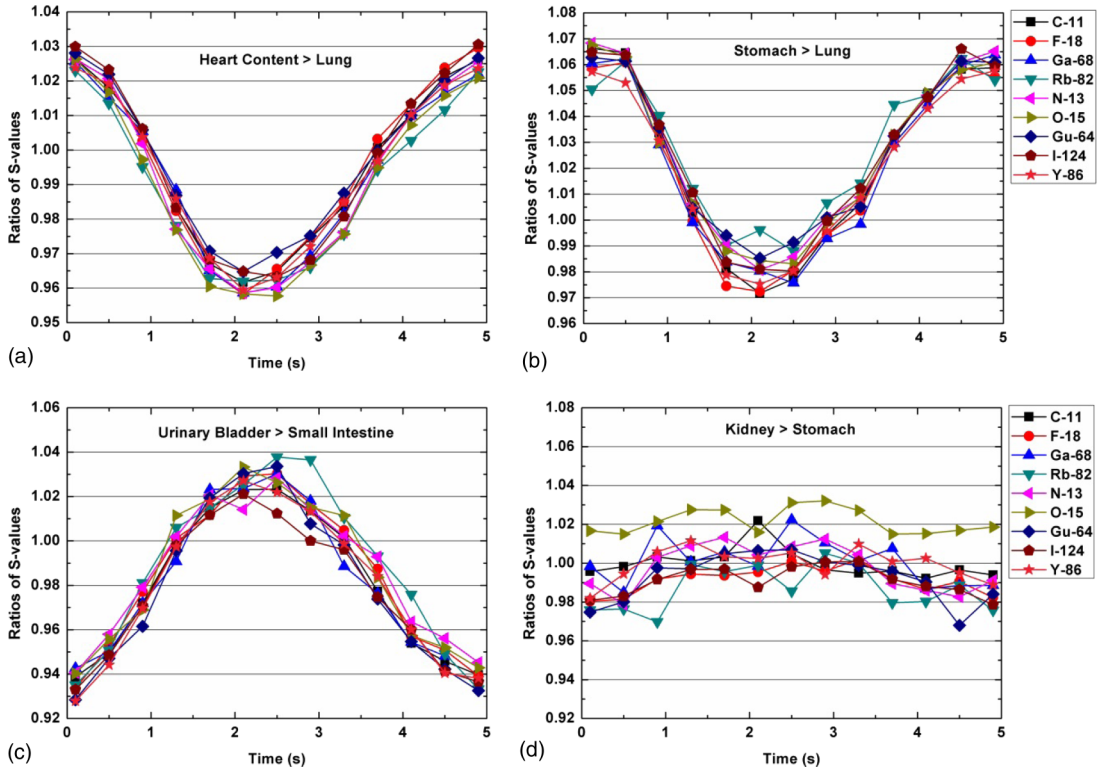

FIG. 7. Ratios of cross S-values for (a) the heart contents irradiating the lung, (b) the stomach irradiating the lung, (c) the urinary bladder irradiating the small intestine, and (d) the kidney irradiating the stomach between the dynamic phantoms and the static phantoms during an average respiratory cycle of 5.2 s, starting from the beginning of inhalation to the end of exhalation.

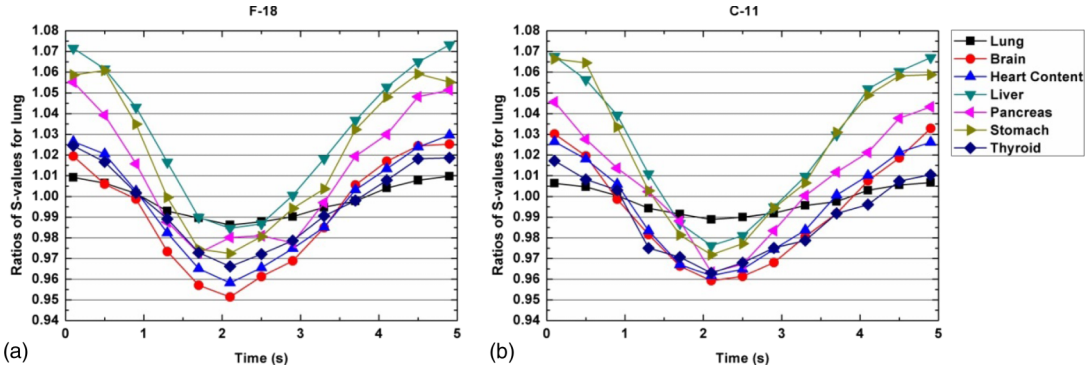

FIG. 8. Ratios of S-values of (a) F-18 and (b) C-11 for selected source organs irradiating the lung between the dynamic phantoms and the static phantoms during an average respiratory cycle of 5.2 s, starting from the beginning of inhalation to the end of exhalation.

can be explained by the fact that the inhaled air in the lung facilitates the penetration of 511 keV photons while the expanded lung absorbs more energy from the nonpenetrating positrons.

3.D. Effect of respiratory motion on organ absorbed dose

The absorbed dose of ^{18}F-FDG in the static and dynamic phantoms was calculated based on the estimated S-values of F-18 and the reported time-dependent biodistribution data, according to Eqs. (1) and (2), respectively. Comparison of the results obtained using static and dynamic phantoms with those reported by Zankl *et al.*[17] is given in Table IV. For each considered organ, the absorbed doses of ^{18}F-FDG in the static and dynamic phantoms are almost identical. The minor differences between the results of the dynamic phantom and Zankl *et al.*[17] can be attributed to the anatomic dissimilarity between the different computational phantoms. The phantom of Zankl *et al.*[17] was constructed from CT data of a 38-yr-old patient and modified according to the anatomical configuration of the ICRP adult reference male, while the XCAT phantom was based on the Visible Human anatomical dataset of the National Library of Medicine.

For all considered organs, the absolute difference of absorbed dose between the static and dynamic phantoms is less than 2.5%. The absorbed dose of ^{18}F-FDG is less influenced by respiratory motion because the mean residence time of ^{18}F-FDG in the lung is relatively short compared to other source organs and the cumulated activity in the different organs compensates for the S-value induced discrepancy of absorbed dose. This work focused mostly on radiotracers used in diagnostic imaging procedures where the radiation dose is small and, as such, the biological impact of respiration-induced differences is small. However, the same holds true for therapeutic procedures involving the use of high activities, especially for radiopharmaceuticals with long residence time in the lung and epigastric organs (e.g., I-131 or Y-90) which may cause higher organ dose differences.

4. CONCLUSION

In most internal dosimetry studies, dose calculations are usually performed on static computational phantoms,[18–25] which disregard respiratory motion and, as such, are not able to describe the motion correlated and time varying dose distribution. Accordingly, respiration-induced changes in internal organ doses merit evaluation using 4D anatomical models.

A systematic study was performed to assess the impact of respiratory motion on the dosimetric properties of monoenergetic photons and electrons and common positron-emitting radionuclides using an anthropomorphic model of the adult man. The self-absorbed SAFs of most organs/tissues are less

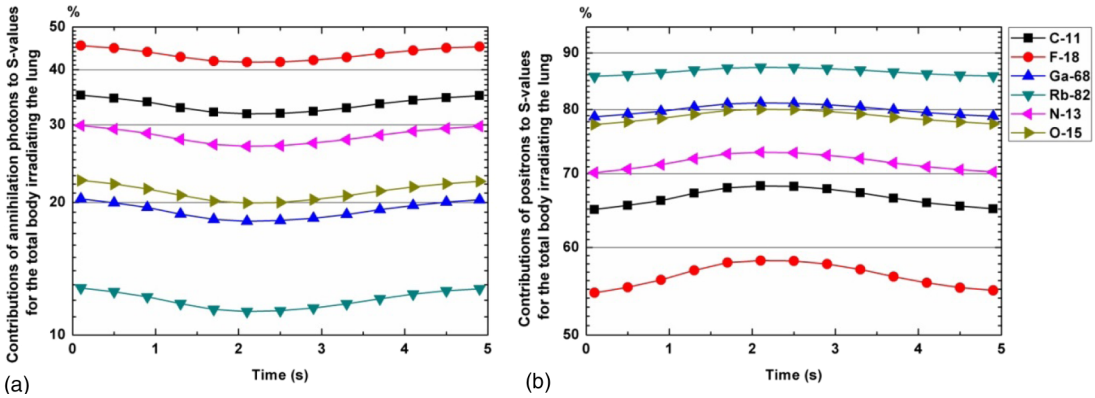

FIG. 9. The contributions of (a) annihilation photons and (b) positrons to the total S-values of selected radionuclides of the total body irradiating the lung in the dynamic phantoms for one respiratory cycle.

TABLE IV. Comparison of absorbed dose of selected organs from ^{18}F-FDG between the static phantoms, dynamic phantoms, and results reported by Zankl *et al.* (Ref. 17).

	Absorbed dose from ^{18}F-FDG (mGy/MBq)		
Organs	Static phantoms	Dynamic phantoms	Zankl *et al.* (Ref. 17)
Adrenal	1.18×10^{-2}	1.15×10^{-2}	1.25×10^{-2}
Brain	2.48×10^{-2}	2.48×10^{-2}	3.55×10^{-2}
Colon	1.11×10^{-2}	1.10×10^{-2}	1.19×10^{-2}
Heart wall	4.26×10^{-2}	4.20×10^{-2}	6.16×10^{-2}
Kidney	1.07×10^{-2}	1.07×10^{-2}	1.17×10^{-2}
Liver	1.50×10^{-2}	1.49×10^{-2}	2.20×10^{-2}
Lung	9.76×10^{-3}	9.75×10^{-3}	1.89×10^{-2}
Pancreas	1.18×10^{-2}	1.17×10^{-2}	1.28×10^{-2}
Small intestine	1.05×10^{-2}	1.05×10^{-2}	1.30×10^{-2}
Spleen	9.87×10^{-3}	9.89×10^{-3}	1.14×10^{-2}
Stomach	1.19×10^{-2}	1.19×10^{-2}	1.23×10^{-2}
Thymus	1.13×10^{-2}	1.12×10^{-2}	1.18×10^{-2}
Thyroid	8.68×10^{-3}	8.68×10^{-3}	1.00×10^{-2}
Testes	9.15×10^{-3}	9.02×10^{-3}	9.64×10^{-3}
Prostate	2.93×10^{-2}	2.90×10^{-2}	2.63×10^{-2}
Esophagus	1.19×10^{-2}	1.20×10^{-2}	1.50×10^{-2}
Skin	7.00×10^{-3}	7.01×10^{-3}	7.17×10^{-3}

influenced by respiratory motion. However, the respiration-induced volume variation of the lung and the positioning movement of internal organs during respiration create perceptible effects on the self-absorbed dose for the lung and cross dose for some source-target organ pairs. Although the comparison between the static and dynamic models for ^{18}F-FDG showed negligible effect of respiration motion on the calculated absorbed doses, further investigation using other radiotracers is recommended. Overall, it can be concluded that for internal radiation dosimetry calculations, respiration-induced uncertainty is less than 10%. In this regard, a dynamic computational model can provide more accurate assessment of radiation dose to the lung and abdominal organs than a conventional static phantom.

ACKNOWLEDGMENTS

This work was supported by the Swiss National Science Foundation under Grant No. SNSF 31003A-149957 and Geneva Cancer League.

[a]Author to whom correspondence should be addressed. Electronic mail: habib.zaidi@hcuge.ch; Telephone: +41 22 372 7258; Fax: +41 22 372 7169.

[1]H. Zaidi and X. G. Xu, "Computational anthropomorphic models of the human anatomy: The path to realistic Monte Carlo modeling in medical imaging," Annu. Rev. Biomed. Eng. **9**, 471–500 (2007).
[2]X. G. Xu and K. F. Eckerman, *Handbook of Anatomical Models for Radiation Dosimetry* (CRC, Boca Raton, FL, 2009), p. 576.
[3]H. Zaidi, "Relevance of accurate Monte Carlo modeling in nuclear medical imaging," Med. Phys. **26**, 574–608 (1999).
[4]T. G. Purdie, D. J. Moseley, J. P. Bissonnette, M. B. Sharpe, K. Franks, A. Bezjak, and D. A. Jaffray, "Respiration correlated cone-beam computed tomography and 4DCT for evaluating target motion in stereotactic lung radiation therapy," Acta. Oncol. **45**, 915–922 (2006).
[5]J. Zhang, G. X. Xu, C. Shi, and M. Fuss, "Development of a geometry-based respiratory motion-simulating patient model for radiation treatment dosimetry," J. Appl. Clin. Med. Phys. **9**, 16–28 (2008).
[6]ICRP, "The 2007 recommendations of the international commission on radiological protection," Ann. ICRP **37**, 1–332 (2007).
[7]B. Roswit and D. C. White, "Severe radiation injuries of the lung," AJR, Am. J. Roentgenol. **129**, 127–136 (1977).
[8]R. A. Castellino, E. Glatstein, M. M. Turbow, S. Rosenberg, and H. S. Kaplan, "Latent radiation injury of lungs or heart activated by steroid withdrawal," Ann. Intern. Med. **80**, 593–599 (1974).
[9]ICRP, "Basic anatomical and physiological data for use in radiological protection: Reference values," Ann. ICRP **32**, 1–277 (2002).
[10]W. E. Bolch, K. F. Eckerman, G. Sgouros, and S. R. Thomas, "MIRD Pamphlet No. 21: A generalized schema for radiopharmaceutical dosimetry—Standardization of nomenclature," J. Nucl. Med. **50**, 477–484 (2009).
[11]W. P. Segars, G. Sturgeon, S. Mendonca, J. Grimes, and B. M. Tsui, "4D XCAT phantom for multimodality imaging research," Med. Phys. **37**, 4902–4915 (2010).
[12]D. B. Pelowitz, MCNPX User's Manual Version 2.5.0., Los Alamos National Laboratory, Report No. LA-CP-05–0369, 2005.
[13]M. G. Stabin and J. A. Siegel, "Physical models and dose factors for use in internal dose assessment," Health Phys. **85**, 294–310 (2003).
[14]T. Chao, "The development and application of a tomographic whole-body model for Monte Carlo organ dose calculation," Ph.D. thesis, Rensselaer Polytechnic Institute, NY, 2001.
[15]Health Physics Society, http://hps.org/publicinformation/radardecaydata.cfm, 2013.
[16]L. G. Bouchet, W. E. Bolch, H. P. Blanco, B. W. Wessels, J. A. Siegel, D. A. Rajon, I. Clairand, and G. Sgouros, "MIRD Pamphlet No 19: Absorbed fractions and radionuclide S values for six age-dependent multiregion models of the kidney," J. Nucl. Med. **44**, 1113–1147 (2003), http://jnm.snmjournals.org/content/44/7/1113.long.
[17]M. Zankl, H. Schlattl, N. Petoussi-Henss, and C. Hoeschen, "Electron specific absorbed fractions for the adult male and female ICRP/ICRU reference computational phantoms," Phys. Med. Biol. **57**, 4501–4526 (2012).
[18]M. G. Stabin, R. B. Sparks, and E. Crowe, "OLINDA/EXM: The second-generation personal computer software for internal dose assessment in nuclear medicine," J. Nucl. Med. **46**, 1023–1027 (2005), http://jnm.snmjournals.org/content/46/6/1023.long.
[19]W. Bolch, C. Lee, M. Wayson, and P. Johnson, "Hybrid computational phantoms for medical dose reconstruction," Radiat. Environ. Biophys. **49**, 155–168 (2010).
[20]C. Y. Shi, X. G. Xu, and M. G. Stabin, "SAF values for internal photon emitters calculated for the RPI-P pregnant-female models using Monte Carlo methods," Med. Phys. **35**, 3215–3224 (2008).
[21]M. Zankl, N. Petoussi-Henss, U. Fill, and D. Regulla, "The application of voxel phantoms to the internal dosimetry of radionuclides," Radiat. Prot. Dosim. **105**, 539–547 (2003).
[22]N. Petoussi-Henss and M. Zankl, "Voxel anthropomorphic models as a tool for internal dosimetry," Radiat. Prot. Dosim. **79**, 415–418 (1998).
[23]T. Xie, W. E. Bolch, C. Lee, and H. Zaidi, "Pediatric radiation dosimetry for positron-emitting radionuclides using anthropomorphic phantoms," Med. Phys. **40**, 102502 (13pp.) (2013).
[24]T. Xie and H. Zaidi, "Evaluation of radiation dose to anthropomorphic paediatric models from positron-emitting labelled tracers," Phys. Med. Biol. **59**, 1165–1187 (2014).
[25]T. Xie and H. Zaidi, "Fetal and maternal absorbed dose estimates for positron-emitting molecular imaging probes," J. Nucl. Med. **55**, 1459–1466 (2014).